Dalton Transactions

ROYAL SOCIETY OF CHEMISTRY

PAPER

View Article Online
View Journal | View Issue

Cite this: *Dalton Trans.*, 2024, **53**, 3825

Luminescent lanthanide complexes based on 4,5-di(3,5-dicarboxylphenoxy)phthalic acid as enhanced fluorescence probes for highly selective detection of lead(II) ions in water†

Wenwen Wei [a] Ai Wang [a] Liping Lu [a] Caixia Yuan *[a] Sisi Feng *[a,b] Ulli Englert [a] and Shengqian Ma *[c]

Received 9th December 2023,
Accepted 29th January 2024

DOI: 10.1039/d3dt04118b

rsc.li/dalton

Six novel lanthanide complexes ($[Nd_2(L)(H_2O)_6]_n{\cdot}4.58n(H_2O)$ (**1**), $[Ln(H_3L)(H_2O)]_n{\cdot}0.5n(H_2O)$, Ln = Sm (**2**), Eu (**3**), Gd (**4**), Tb (**5**), $Eu_{0.18}Gd_{0.62}Tb_{0.20}$ (**6**)) have been hydrothermally synthesized based on the ligand 4,5-di(3,5-dicarboxylphenoxy)phthalic acid (H_6L). Single crystal X-ray diffraction reveals that complexes **1–6** are 2D structures, where **2–6** are isomorphic. Complexes **3** and **5** exhibit the characteristic fluorescence of Eu(III) and Tb(III) ions respectively, while complex **4** shows blue-green light emission based on the ligand. In particular, the ternary Eu/Gd/Tb complex **6** shows white light emission with a CIE (Commission International del'Eclairage) chromaticity coordinate of (0.330, 0.339) and hence close to pure white light emission. Moreover, complexes **3** and **5** display specific fluorescence-enhanced detection performance for Pb^{2+} ions: The interaction between Pb^{2+} ions and the ligand enhances the charge transfer efficiency between the ligand and the Eu(III) and Tb(III) ions and thus leads to fluorescence enhancement of complexes **3** and **5**. More importantly, complex **3** exhibits the lowest detection limit of 4.72 nM for Pb^{2+} ions among the existing complex fluorescent probes. In addition, both complexes **3** and **5** show good performance for recycling and for the detection of Pb^{2+} in real water samples.

1. Introduction

Lead ions (Pb^{2+}) are widely encountered in daily life; they occur in batteries, toy jewelry, pigments, *etc.*[1–7] Pb^{2+} represents one of the most toxic heavy metal ions and is highly hazardous to human health. After intake into the human body it can damage the functions of the kidneys, the reproductive and nervous system, and brain cells.[8–14] Therefore, reliable methods for the detection of Pb^{2+} ions are urgently needed. The scientific literature suggests that most of the materials used for fluorescence detection of Pb^{2+} ions are based on rather expensive carbon quantum dot-doped metal gold.[15–18] In a more general context, lanthanide complexes are widely used as fluorescent sensing materials because of their unique 'antenna effect' and their colors visible to the naked eye.[19–22] The 'antenna effect' of lanthanide fluorescent materials is often attenuated or even annihilated by the encountered fluorescence resonance energy transfer (FRET) and photoinduced electron transfer (PET) mechanisms, and therefore most lanthanide complexes exhibit 'turn-off' fluorescent probes.[23,24] In contrast, enhanced fluorescent probes show higher sensitivity due to reduced background interference and a higher signal-to-noise ratio.[13,25–29] Therefore, the study of lanthanide complexes with enhanced fluorescence sensing properties and their fluorescence enhancement mechanisms have attracted much attention.

Aromatic polycarboxylic acid ligands including ether bonds appear particularly attractive: these flexible σ bonds can reduce steric hindrance by free rotation and maximizing the coordination requirements of metal ions.[30–36] Moreover, the ether bonds may interact with metal ions as additional Lewis basic sites to achieve the identification of metal ions with precision.[37–41] Herein, we report six two-dimensional (2D) and structurally novel complexes **1–6** ($[Nd_2(L)(H_2O)_6]_n{\cdot}4.58n(H_2O)$ (**1**), $[Ln(H_3L)(H_2O)]_n{\cdot}0.5n(H_2O)$, Ln = Sm (**2**), Eu (**3**), Gd (**4**), Tb (**5**), $Eu_{0.18}Gd_{0.62}Tb_{0.20}$ (**6**)), which are constructed by the aromatic polycarboxylic acid ligand 4,5-di(3,5-dicarboxylphenoxy)

[a]*Institute of Molecular Science, Key Laboratory of Chemical Biology and Molecular Engineering of the Education Ministry, Shanxi University, Taiyuan, Shanxi 030006, People's Republic of China. E-mail: cxyuan@sxu.edu.cn, ssfeng@sxu.edu.cn*
[b]*Key Laboratory of Materials for Energy Conversion and Storage of Shanxi Province, Shanxi University, Taiyuan, Shanxi 030006, People's Republic of China*
[c]*Department of Chemistry, University of North Texas CHEM 305D, 1508 W Mulberry St, Denton, TX, 76201, USA. E-mail: Shengqian.Ma@unt.edu*

†Electronic supplementary information (ESI) available: Materials and physical measurements, Scheme S1, Fig. S1–S10 and Table S1–S4. CCDC 2303091–2303094. For ESI and crystallographic data in CIF or other electronic format see DOI: https://doi.org/10.1039/d3dt04118b

phthalic acid (H_6L, shown in Scheme S1†) featuring ether bonds. Although some complexes based on H_6L ligand have been reported,[42–44] the ligand exhibits different protonation forms and coordination modes due to the different type and coordination environment of metal ions, resulting in structural diversity and property difference of the complexes. The structural and fluorescence properties of **1–6** have been studied in detail. Considering the unique luminescence of Eu/Gd/Tb complexes, the co-doped trimetallic complex **6** with white light emission was synthesized. In addition, complexes **3** and **5** were investigated as enhanced fluorescent probes for the specific detection of Pb^{2+} ions, and the fluorescence detection mechanism was analyzed in detail.

2. Experimental

2.1 Synthesis of $[Nd_2(L)(H_2O)_6]_n \cdot 4.58n(H_2O)$ (1)

As shown in Scheme S1,† the syntheses of all complexes only differ by the initial lanthanide salts. A mixture of $NdCl_3 \cdot 6H_2O$ (53.80 mg, 0.15 mmol), H_6L (26.30 mg, 0.05 mmol) and H_2O (8 mL) was sealed in a 15 mL Teflon-lined stainless steel container. The autoclave was heated under autogenous pressure at 413 K for 72 h and then allowed to cool to room temperature. Colorless spindle-shaped crystals of **1** were obtained by filtration, washed with water and dried in air. Yield 9% (based on H_6L). Elemental analysis calculated (%) for $C_{24}H_{29.23}Nd_2O_{24.60}$: C 28.83, H 2.95; found: C 28.80, H 2.96. IR (KBr, ν, cm^{-1}): 3428 (m), 1621 (m), 1543 (s), 1394 (s), 1316 (m), 1265 (m), 1174 (s), 1102 (w), 1053 (m), 981 (s), 825 (s), 782 (s), 732 (w), 668 (w), 612 (w).

2.2 Synthesis of $[Sm(H_3L)(H_2O)]_n \cdot 0.5n(H_2O)$ (2)

The procedure was the same as that of **1** except that $NdCl_3 \cdot 6H_2O$ was replaced by $SmCl_3 \cdot 6H_2O$ (54.72 mg, 0.15 mmol). Massive colorless bulk crystals of **2** were obtained, yield 60% based on H_6L. Elemental analysis calculated (%) for $C_{24}H_{14}SmO_{15.5}$: C 41.14, H 2.01; found: C 41.18, H 2.06. IR (KBr, ν, cm^{-1}): 3371 (m), 3080 (w), 2924 (w), 2852 (w), 2568 (w), 1707 (s), 1572 (s), 1423 (s), 1294 (s), 1223 (m), 1174 (s), 1053 (w), 981 (s), 910 (s), 796 (m), 768 (m), 704 (s), 661 (s), 618 (s).

2.3 Synthesis of $[Eu(H_3L)(H_2O)]_n \cdot 0.5n(H_2O)$ (3)

The procedure was the same as that of **1** except that $NdCl_3 \cdot 6H_2O$ was replaced by $EuCl_3 \cdot 6H_2O$ (54.95 mg, 0.15 mmol). Colorless bulk crystals of **3** were obtained, yield 57%. Elemental analysis calculated (%) for $C_{24}H_{14}EuO_{15.5}$: C 40.04, H 2.01; found: C 40.01, H 2.07. IR (KBr, ν, cm^{-1}): 3371 (m), 3080 (w), 2924 (w), 2852 (w), 2568 (w), 1707 (s), 1572 (s), 1423 (s), 1294 (s), 1223 (m), 1174 (s), 1053 (w), 981 (s), 910 (s), 796 (m), 768 (m), 704 (s), 661 (s), 618 (s).

2.4 Synthesis of $[Gd(H_3L)(H_2O)]_n \cdot 0.5n(H_2O)$ (4)

The procedure was the same as that of **1** except that $NdCl_3 \cdot 6H_2O$ was replaced by $GdCl_3 \cdot 6H_2O$ (55.76 mg, 0.15 mmol). Colorless bulk crystals of **4** were obtained, yield 59%. Elemental analysis calculated (%) for $C_{24}H_{14}GdO_{15.5}$: C 40.74, H 1.99; found: C 40.69, H 2.01. IR (KBr, ν, cm^{-1}): 3371 (m), 3080 (w), 2924 (w), 2852 (w), 2568 (w), 1707 (s), 1572 (s), 1423 (s), 1294 (s), 1223 (m), 1174 (s), 1053 (w), 981 (s), 910 (s), 796 (m), 768 (m), 704 (s), 661 (s), 618 (s).

2.5 Synthesis of $[Tb(H_3L)(H_2O)]_n \cdot 0.5n(H_2O)$ (5)

The procedure was the same as that of **1** except that $NdCl_3 \cdot 6H_2O$ was replaced by $TbCl_3 \cdot 6H_2O$ (56.01 mg, 0.15 mmol). Colorless bulk crystals of **5** were obtained, yield 63%. Elemental analysis calculated (%) for $C_{24}H_{14}TbO_{15.5}$: C 40.64, H 1.99; found: C 40.60, H 2.02. IR (KBr, ν, cm^{-1}): 3371 (m), 3080 (w), 2924 (w), 2852 (w), 2568 (w), 1707 (s), 1572 (s), 1423 (s), 1294 (s), 1223 (m), 1174 (s), 1053 (w), 981 (s), 910 (s), 796 (m), 768 (m), 704 (s), 661 (s), 618 (s).

2.6 Synthesis of $[Eu_{0.18}Gd_{0.62}Tb_{0.20}(H_3L)(H_2O)]_n \cdot 0.5n(H_2O)$ (6)

Complex **6** was synthesized by the same method as **1–5** but from a mixture of $EuCl_3 \cdot 6H_2O$, $GdCl_3 \cdot 6H_2O$ and $TbCl_3 \cdot 6H_2O$ as lanthanide sources. ICP analyses confirmed that the relative molar ratios of Eu/Gd/Tb within the doped complex **6** correspond to that of the reaction stoichiometry. Powder X-ray diffraction (PXRD) proved that **2–5** and the ternary complex **6** are isostructural. Colorless bulk crystals of **6** were obtained, yield 55%. Elemental and inductively coupled plasma (ICP) analysis calculated (%) for $C_{24}H_{14}Eu_{0.18}Gd_{0.62}Tb_{0.20}O_{15.5}$: C 40.77, H 2.00, Eu^{3+}: 0.20, Gd^{3+}: 0.62, Tb^{3+}: 0.18; found: C 40.71, H 2.07, Eu^{3+}: 0.18, Gd^{3+}: 0.62, Tb^{3+}: 0.20. IR (KBr, ν, cm^{-1}): 3371 (m), 3080 (w), 2924 (w), 2852 (w), 2568 (w), 1707 (s), 1572 (s), 1423 (s), 1294 (s), 1223 (m), 1174 (s), 1053 (w), 981 (s), 910 (s), 796 (m), 768 (m), 704 (s), 661 (s), 618 (s).

2.7 X-ray crystallography

Crystallographic data of complexes **1**, **2**, **4** and **5** were collected on a Bruker D8-Quest diffractometer equipped with a Photon 100 detector and Mo-Kα radiation (λ = 0.71073 Å, graphite monochromator) at room. The multi-scan approach was applied for absorption corrections.[45] The structures of complexes **1**, **2**, **4** and **5** were solved by Intrinsic Phasing[46] within the Olex2 program[47] and refined on F^2 with the full-matrix least-squares technique using the SHELXL-2018 program.[48] With the exception of a few disordered atoms, anisotropic displacement parameters were assigned to non-H atoms, and hydrogen atoms attached to carbon were added in ideal positions and refined by a riding model. H atoms attached to oxygen were located from different Fourier maps and refined as riding in idealized positions (O–H distances 0.81–0.90 Å), with $U_{iso}(H) = 1.5U_{eq}(O)$. Crystal data and structure refinement details of complexes **1**, **2**, **4** and **5** are summarized in Table S1.†

2.8 Fluorescence detection experiment

A powder sample of the complex under study (2 mg) was dispersed in 50 mL distilled water, treated with ultrasound for 30 minutes and set for 3 days. The supernatant was used for the fluorescence detection experiments. In a first step, the supernatant of the complex (2 mL) was used to measure the fluorescence spectrum and to determine the optimum exci-

tation and emission wavelength. In a second step, aqueous solutions of different cations and anions (200 μL, 1 mM, Na^+, Mg^{2+}, K^+, Ca^{2+}, Cr^{3+}, Mn^{2+}, Fe^{2+}, Fe^{3+}, Co^{2+}, Ni^{2+}, Cu^{2+}, Cu^+, Zn^{2+}, Pb^{2+}, Ag^+, Cd^{2+}, Hg^{2+}, Hg^+, Ba^{2+}, F^-, Cl^-, Br^-, I^-, Ac^-, NO_3^-, $H_2PO_4^-$, CO_3^{2-}, HCO_3^-, $C_2O_4^{2-}$, SO_4^{2-}, CrO_4^{2-}, $Cr_2O_7^{2-}$, MoO_4^{2-}, BO_3^{3-}, PO_4^{3-}) were added to the supernatant of the complex and the fluorescence spectra were recorded.

3. Results and discussion

3.1 Crystal structure of complex 1

Single crystal X-ray diffraction analysis showed that complex **1** crystallized in the monoclinic space group $P2_1/c$. The asymmetric unit of complex **1** contains two Nd(III) ions, a fully deprotonated L^{6-} ligand, six coordinated and 4.58 uncoordinated water molecules. As shown in Fig. 1, the Nd1 ion in complex **1** adopts a nine-coordinated tricapped trigonal prismatic geometry, in which six oxygen atoms (O3, O4, $O5^i$, $O6^i$, $O7^{ii}$, $O8^{ii}$) are derived from three different L^{6-} ligands, and three oxygen atoms (O15, O16, O17) are derived from three coordinated water molecules. Atom Nd2 is ten-coordinated in bicapped tetragonal antiprismatic geometry with seven oxygen atoms ($O1^i$, $O2^i$, $O2^{iii}$, $O9^{iv}$, $O10^{iv}$, O11, O12) from four different L^{6-}ligands and three oxygen atoms (O18, O19, O20) from three coordinated water molecules. The length of the Nd–O bonds ranges from 2.433(6) to 2.889(7) Å.

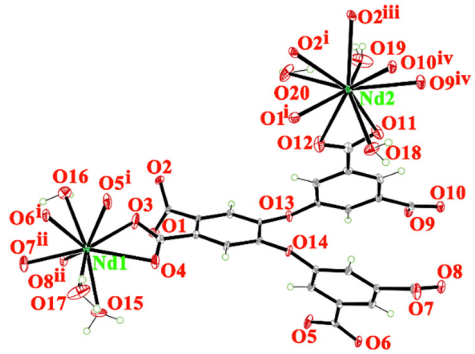

Fig. 1 Coordination environments of Nd(III) ions in complex **1**, symmetry codes: (i) *x*, 1/2 − *y*, 1/2 + *z*; (ii) *x*, −1 + *y*, *z*; (iii) −*x*, 1/2 + *y*, 1.5-*z*; (iv) *x*, 1.5 − *y*, 1/2 + *z*.

As shown in Fig. 2a, each L^{6-} ligand connects seven Nd(III) ions in a μ_7-η^2:η^1:η^1:η^1:η^1:η^1:η^1:η^1:η^1:η^1 coordination mode in complex **1**. The bond angles of the two ether bonds C–O–C in ligand L^{6-} are 122.3 (6) and 119.3(6)°. The dihedral angles between the benzene rings are 58.3(2)° for *Cg*1 (C2–C7) and *Cg*2 (C9–C14), 58.4(2)° for *Cg*1 and *Cg*3 (C17–C22), and 19.6 (2)° for *Cg*2 and *Cg*3. Fig. 2b shows the one-dimensional (1D) chain structure of complex **1** along the *b*-axis. The coordination water molecules prevent the extension of complex **1** towards the *a*-axis, giving the complex the two-dimensional (2D) planar structure as shown in Fig. 2c. To get better insight into the network of complex **1**, Nd1, Nd2 and ligand L^{6-} can be simplified as 3-, 5- and 7-connected nodes, respectively, and the whole network can be treated as a (3,5,7) connected structure with the point symbol $\{3{\cdot}4^7{\cdot}5^5{\cdot}6^5{\cdot}7^3\}\{3^2{\cdot}4^5{\cdot}5^3\}\{4^3\}$ (Fig. 2d). Further, intermolecular hydrogen bonds (O15–H15*A*···$O1^i$, O18–H18*A*···$O8^{ii}$, O18–H18*B*···O25 and O26–H26*B*···O24 (symmetry codes: (i) −*x* + 1, −*y*, −*z* + 1; (ii) *x*, −*y* + 3/2, *z* + 1/2)) connect the adjacent planar layers into a three-dimensional (3D) network (Fig. 2e). In addition, the stability of the framework structure is further enhanced by π···π stacking interactions between adjacent rings. As shown in Fig. 2f, the distance between *Cg*2 and *Cg*3 is 3.738(4) Å and the distance

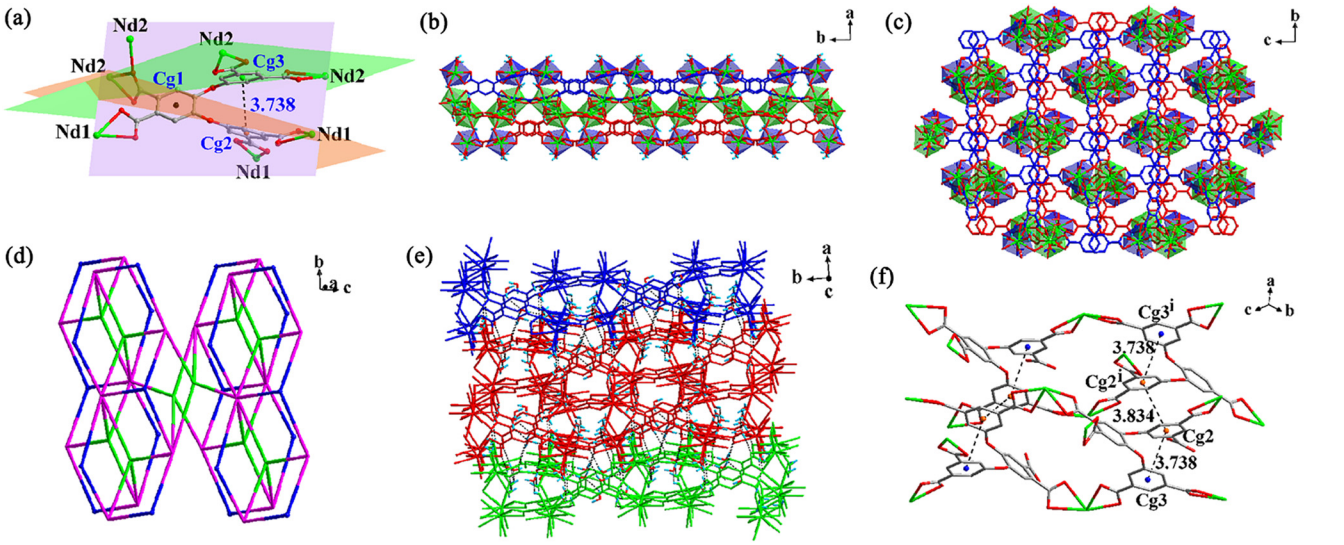

Fig. 2 (a) Coordination mode of the ligand L^{6-} in **1** (the sky blue represents H atom; the three different colored planes represent the planes of the three benzene rings in the ligand); (b) 1D chain structure; (c) 2D structure; (d) Topological structure; (e) 3D network formed by hydrogen bonds; (f) π···π interactions present in complex **1**.

between *Cg*2 and *Cg*2^{i} is 3.834(3) Å (symmetry code: (i) 1 − *x*, 1 − *y*, 1 − *z*).

3.2 Crystal structures of complexes 2–6

The crystallographic results reveal that complexes **2–6** are isostructural and crystallize in the triclinic space group $P\bar{1}$ of the triclinic system. Herein, the structure of complex **5** is described in detail as a representative of this group. The asymmetric unit of complex **5** contains one Tb(III) ion, one partially deprotonated H_3L^{3-} ligand, one coordinated and one-half of free water molecule. As shown in Fig. 3a, each Tb(III) ion is eight coordinated with a bi-capped trigonal prismatic geometry by seven oxygen atoms (O1^{iv}, O2^{iv}, O3^{ii}, O7^{iii}, O8^{iii}, O9^{i}, O10) from five H_3L^{3-} ligands and one oxygen atom (O15) from a coordinated water molecule. The Tb–O bond distances range from 2.258(4) to 2.472(4) Å. As shown in Fig. 3b, every H_3L^{3-} ligand bridges five Tb(III) ions in a μ_5-η^1:η^0:η^1:η^1:η^1:η^1:η^0:η^0:η^0:η^0:η^1:η^1 coordination mode to form a 2D sheet. The angles of the two ether bonds C–O–C in the ligand H_3L^{3-} amount to 114.1(4) and 118.7(4)°. In addition, the dihedral angles between the benzene rings *Cg*1 (C1–C6) and *Cg*2 (C9–C14), *Cg*1 and *Cg*3 (C17–C22), *Cg*2 and *Cg*3 are 87.4(2)°, 72.8(2)° and 20.9(2)°, respectively. Fig. 3c and d show the 1D chain structure along the *b*-axis and the 2D planar structure of complex **5**, respectively. The topology of the network thus obtained has been analyzed, taking the Tb(III) ion as a 5-connected node and the ligand H_3L^{3-} as a linker. The overall structure of complex **5** can be perceived as a 5-connected topological network with a point symbol $\{4^8{\cdot}6^2\}$ (Fig. 3e). The adjacent planar layers are connected by intermolecular hydrogen bonds O5–H5···O12^{i} and O11–H11···O6^{i} (symmetric code: (i) −*x* + 2, −*y* + 1, −*z* + 1) to form a 3D network (Fig. 3f). Furthermore, the network is stabilized by π···π stacking between *Cg*2 and *Cg*3 with an inter-ring distance of 3.769(15) Å.

Compared with the Eu^{3+}/Tb^{3+} complexes based on H_6L,[43,44] the ligand in complexes **2–6** has only three carboxyl group deprotonation and still maintains uncoordinated carboxyl oxygen atoms that can further coordinate with other metal ions, so the complexes have the potential to identify metal ions. While in the Eu^{3+}/Tb^{3+} complexes,[43,44] the H_6L ligand is completely deprotonated, and all the carboxyl oxygen atoms participate in the coordination. In addition, the angles between the benzene rings are almost perpendicular to each other, and the distances between adjacent benzene rings are also large, resulting in no π–π interaction in the structure (Fig. S3†), thus affecting the fluorescence properties.

3.3 Infrared spectra

Infrared spectra (IR) of the ligand and all complexes were performed in the range of 4000–400 cm^{-1} (Fig. S4 in ESI†), and they all exhibit a broad peak near 3430 cm^{-1} attributed to the O–H stretching vibration peak of water molecules and hydroxyl groups.[49,50] The peak at 1715 cm^{-1} for the ligand is attributed to the stretching vibration of the protonated carboxyl group, which is weakened in complexes **2–6** and completely absent in complex **1**, suggesting that the carboxyl group in complexes **2–6** is not fully deprotonated, whereas the carboxyl group in complex **1** is completely deprotonated, which is consistent with the results of the single crystal structure analysis.

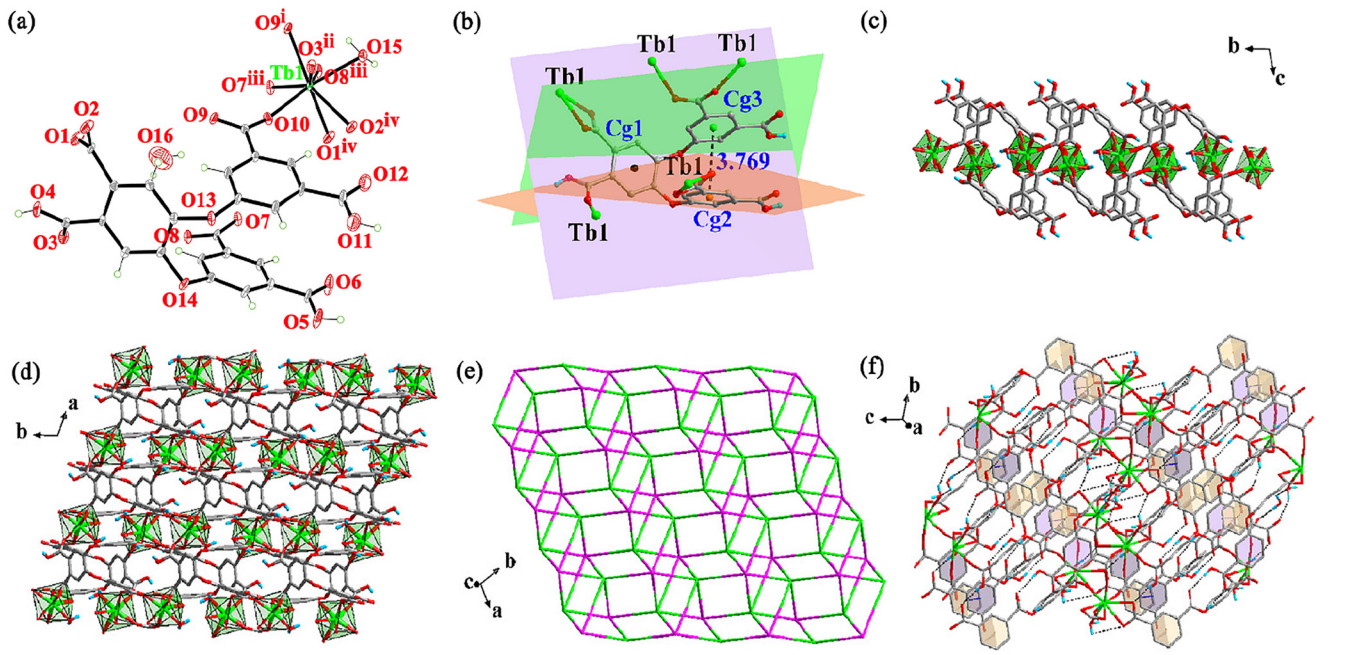

Fig. 3 (a) Coordination environment of Tb(III) ion in complex **5**, symmetry codes: (i) 1 − *x*, 1 − *y*, −*z*; (ii) −1 + *x*, −1 + *y*, *z*; (iii) 2 − *x*, 1 − *y*, −*z*; (iv) *x*, −1 + *y*, *z*; (b) Coordination mode of the ligand H_3L^{3-} in **5** (the sky blue represents H atom; the three different colored planes represent the planes of the three benzene rings in the ligand); (c) 1D chain structure; (d) 2D structure; (e) topological structure; (f) 3D network formed by hydrogen bonding.

3.4 PXRD patterns and thermal analysis

To verify the phase purity of the complexes, the as-synthesized samples were characterized by PXRD at room temperature. Due to the low yield of complex **1**, the properties of **1** have not been studied. As shown in Fig. S5,† the PXRD patterns of complexes **2–6** are in excellent agreement with the simulated one from the crystal structure of **5**, indicating the phase purity of the samples and their isomorphic structures.

In order to investigate the stability of the complexes in water, the powders of complexes **3** and **5** were dispersed in distilled water, ultrasonicated for 30 minutes, and then immersed for three days. The PXRD was performed on the powder samples after natural air drying, and the results were almost identical to the simulated PXRD of the single crystal structure of complex **5** (Fig. S6†), indicating that the structures of complexes **3** and **5** remained stable after immersion in water for three days.

To investigate the thermal stability of the complexes, thermogravimetric analyses (TGA) were performed at a heating rate of 10 °C min^{-1} from RT to 650 °C under an air atmosphere. Since the isomorphic complexes **2–6** displayed similar thermal stability, only complex **5** is discussed in detail. As illustrated in Fig. S7,† the TGA curve shows a gradual loss of one free water molecule (calcd 2.51%, observed 2.75%) in the range of room temperature to 234 °C, and then the structure gradually decomposes.

3.5 Solid-state fluorescence properties

The solid fluorescence spectra of complexes **3–5** and the corresponding chromaticity coordinates according to CIE1931 were measured at room temperature (Fig. 4). Complex **3** shows strong fluorescence emission with four characteristic peaks of Eu(III) ion (λ_{ex} = 330 nm), which is attributed to the $^5D_0 \rightarrow {}^7F_j$ (j = 1, 2, 3, 4) transition of Eu(III) ion, and the $^5D_0 \rightarrow {}^7F_2$ transition at 613 nm is the strongest one with the fluorescence quantum yield of 17.20%. The CIE chromaticity coordinate is (0.566, 0.322), consistent with the red color observed under the ultraviolet lamp. Complex **4** exhibits an emission peak at 496 nm under an excitation of 349 nm with a CIE chromaticity coordinate (0.212, 0.324), showing blue-green light. Compared with the ligand H_6L, the emission peak of **4** exhibits an obvious redshift, which may be caused by the energy transfer of LMCT/LLCT between the ligand and metal ion. When excited at 324 nm, complex **5** displays an intense fluorescence emission spectrum corresponding to the characteristic transitions of $^5D_4 \rightarrow {}^7F_j$ (j = 6, 5, 4, 3) due to the *f–f* transition of Tb(III) ion. The $^5D_4 \rightarrow {}^7F_5$ transition at 543 nm is the strongest one, with a fluorescence quantum yield of 20.96%. The corresponding CIE chromaticity coordinate is (0.292, 0.600), which appears as a green emission, consistent with the color observed under ultraviolet lamps.

3.6 White-light fluorescence of complex 6

Based on the red, blue-green and green light emission of the isomorphic complexes **3–5**, the white light emitting trimetallic complex **6** was obtained by carefully tuning the Eu/Gd/Tb ratio with the RGB (red-green-blue) theory.[51,52] The fluorescence spectra show that the proportion of metal ions and the excitation wavelength would affect the fluorescence emission of the complex. The fluorescence emission spectra of complex **6** at different excitation wavelengths are shown in Fig. 5a. It can be observed that the emission intensity ratio of the $^5D_0 \rightarrow {}^7F_2$ (Eu(III), 613 nm) to $^5D_4 \rightarrow {}^7F_5$ (Tb(III), 543 nm) is gradually increased with the increase of excitation wavelength (Fig. 5b), which indicates that there is an energy transfer from the Tb(III) ion to the Eu(III) ion (Fig. S8†). It corresponds to a shift from yellow-green to white in the CIE chromaticity coordinates (Fig. 5c). The fluorescence emission spectrum of complex **6** at an excitation wavelength of 380 nm is shown in Fig. 5d, where the CIE chromaticity coordinate is (0.330, 0.339), close to the standard white light coordinate (0.333, 0.333). Meanwhile, the fluorescence quantum yield of complex **6** is only 4.86% in the wavelength range of 532 to 628 nm under an excitation of 380 nm, which may be related to the sensitization efficiency of the ligand to Eu(III) and Tb(III) ions. Powder samples of complexes **3–6** under natural light and 365 nm UV lamp irradiation are shown in Fig. 5e. It can be observed that complexes **3–6** exhibit red, blue-green, green and white light emissions, respectively.

3.7 Performance of complexes 3 and 5 for detection of Pb^{2+} ions

In order to investigate the luminescence properties of complexes **3** and **5** in water, fluorescence spectra of suspensions of

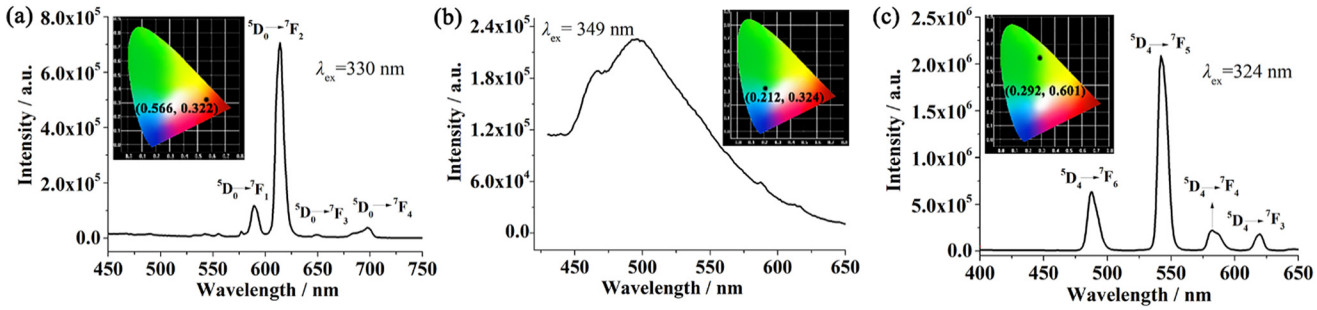

Fig. 4 Solid fluorescence spectra of complexes **3–5** at room temperature (inset: the CIE chromaticity).

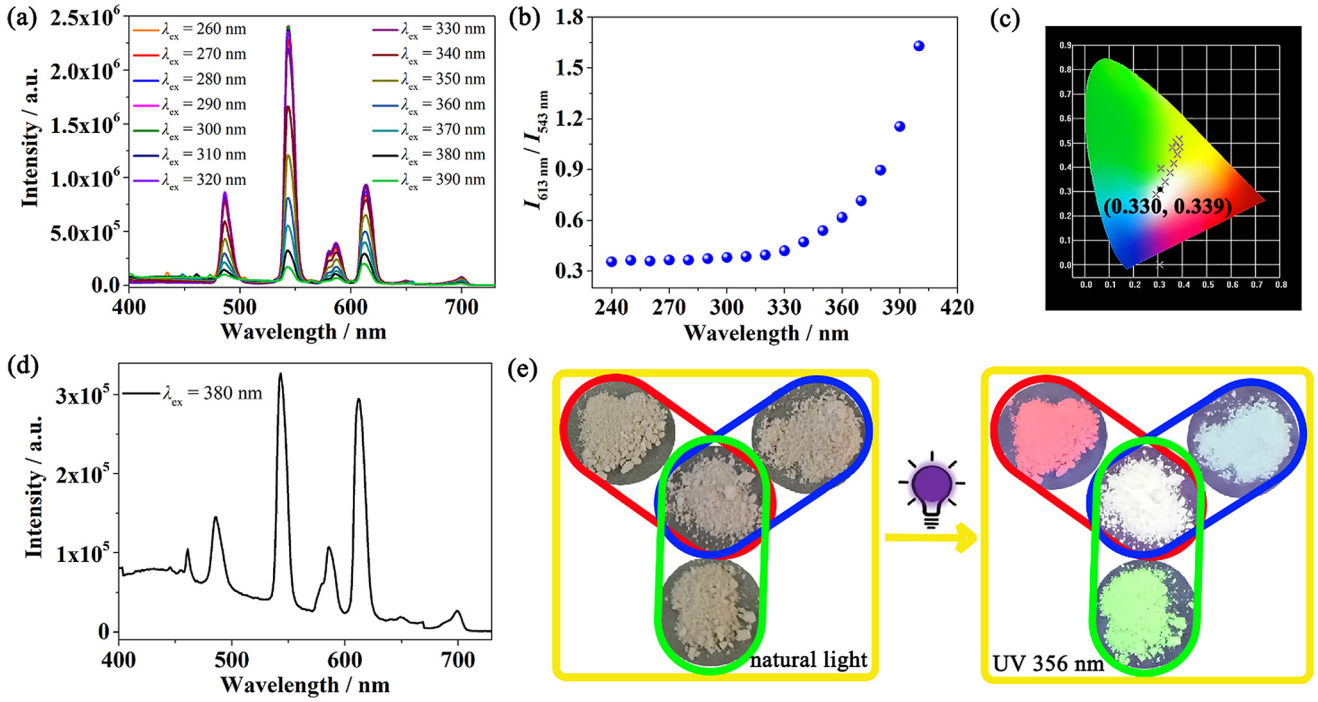

Fig. 5 (a) Solid fluorescence spectra of complex **6** at different excitation wavelengths; (b) Variation curve of $I_{613\ nm}/I_{543\ nm}$ with different excitation wavelengths; (c) CIE coordinates; (d) white light emission spectrum of complex **6** (λ_{ex} = 380 nm); (e) photographs of solid powders of complexes **3**–**6** in natural light and under 365 nm UV light.

complexes **3** and **5** in water were tested. As shown in Fig. 6a and b, both complexes **3** and **5** have optimal emission under excitation at 245 nm. In particular, due to the solvent effect, the energy of the ligand is not fully transferred to the Eu(III) ions when complex **3** is suspended in water, and thus complex **3** retains the fluorescence emission peak of the ligand at 386 nm. In addition, we investigated the fluorescence intensity of complexes **3** and **5** immersed in aqueous solutions of different pH values. As shown in Fig. 6c and d, both complexes **3** and **5** have relatively stable fluorescence intensities in the range of pH = 5–11.

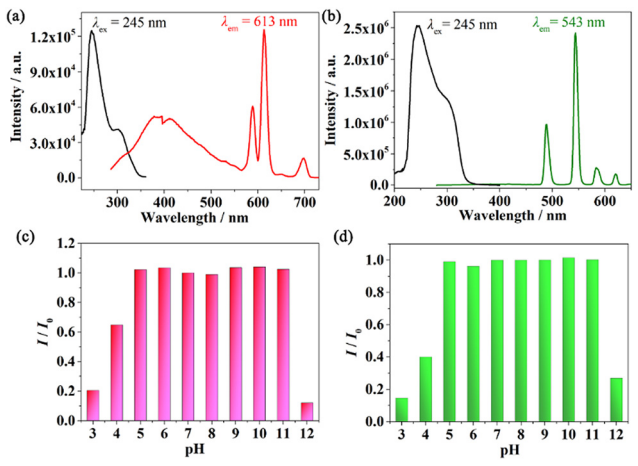

Fig. 6 Fluorescence spectra of complexes (a) **3** and (c) **5** in water; relative fluorescence intensity of complexes (c) **3** and (d) **5** at different pH (λ_{em} = 613 nm for **3**, λ_{em} = 543 nm for **5**).

Considering the excellent fluorescence properties of complexes **3** and **5**, their potential application as fluorescent probes were investigated. The fluorescence intensity of complexes **3** and **5** for various anions and cations was examined under the optimum excitation wavelength of 245 nm. For a clearer view, Fig. 7 shows the relative fluorescence intensity at 613 nm for complex **3** and at 543 nm for complex **5**, respectively. It can be observed that the fluorescence intensities of both complexes **3** and **5** are significantly enhanced upon the addition of Pb^{2+} ions. In particular, the fluorescence quantum yields increase from 0.14% to 1.77% for complex **3** and from 1.36% to 10.98% for complex **5**. Anti-interference experiments were performed to evaluate the detection performance of complexes **3** and **5** on Pb^{2+} in the concomitant presence of competing ions. As displayed in Fig. 8, the fluorescence enhancement effects of Pb^{2+} ions on complexes **3** and **5** are barely affected by the presence of other ions. This indicates that complexes **3** and **5** can be used as enhanced fluorescent probes for the detection of Pb^{2+} ions in aqueous environment without interference from other ions.

To better understand the sensitivity of complexes **3** and **5** toward Pb^{2+} ions, a series of titration experiments were carried out in aqueous solutions with various concentrations of Pb^{2+} ions. As shown in Fig. 9, the fluorescence intensities of complexes **3** and **5** gradually increase with the concentration of

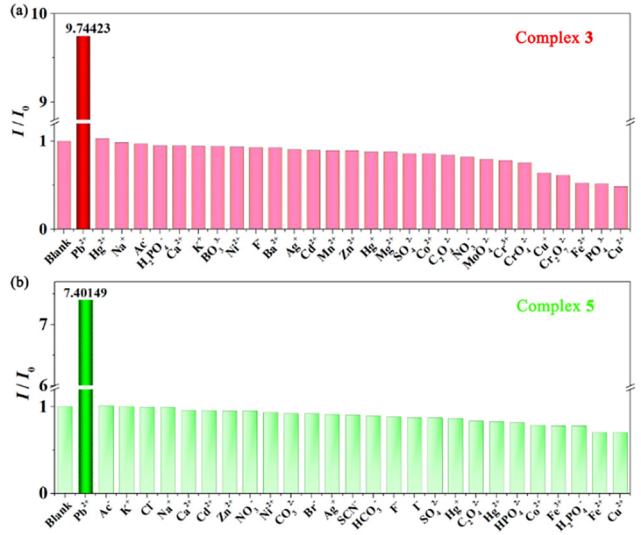

Fig. 7 Relative fluorescence intensity of complexes (b) **3** and (d) **5** (λ_{em} = 613 nm for **3**, λ_{em} = 543 nm for **5**) after the addition of different ions.

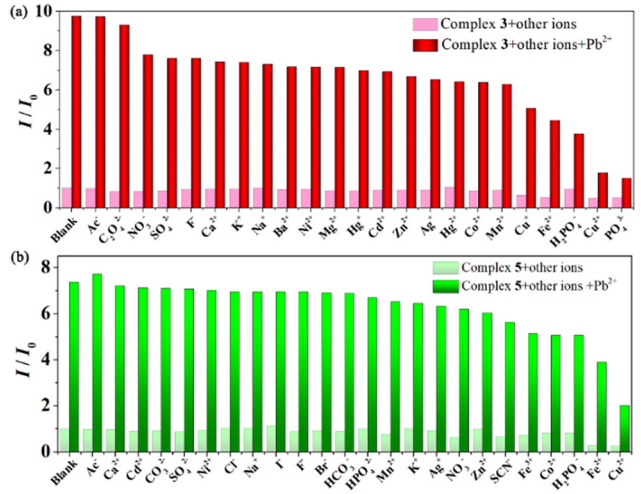

Fig. 8 Relative fluorescence intensity of complexes (a) **3** and (b) **5** after the addition of Pb^{2+} ions in the presence of other ions.

Pb^{2+} ions. The fluorescence intensity of complex **3** reaches a final maximum when the Pb^{2+} ions concentration amounts to 19.6 μM, and a distinct red color is observed under the UV lamp (Fig. 9a inset). Similarly, the fluorescence intensity of complex **5** reaches a maximum for a Pb^{2+} ion concentration of 20 μM, with a distinct green color visible under the UV lamp (Fig. 9c inset). Based on the Stern–Volmer equation $I/I_0 = K_{ec}[M] + 1$,[53] the Stern–Volmer curves of complexes **3** and **5** are almost linear at low concentrations, with correlation coefficients R^2 of 0.9906 and 0.9977, respectively. The enhancement constants K_{ec} are 1.39 × 10^6 M^{-1} and 1.37 × 10^5 M^{-1}, respectively. According to the equation for the limit of detection (LOD) = $3\sigma/k$ (σ is the standard deviation and k is the slope), detection limits of complexes **3** and **5** of 4.72 nM and 49.75 nM, respectively, for Pb^{2+} ions are calculated.

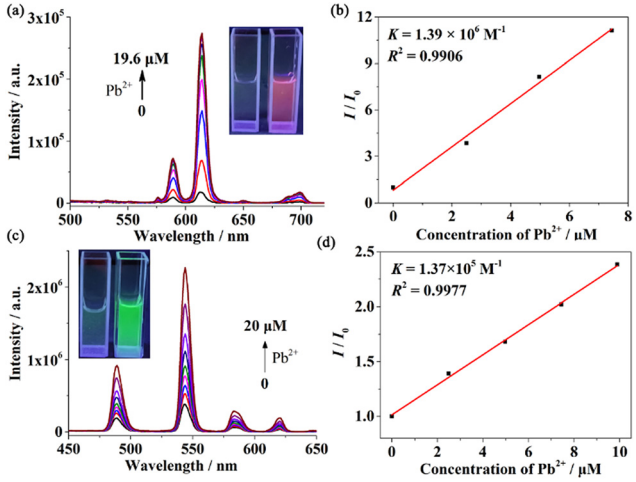

Fig. 9 Fluorescence spectra of complexes (a) **3** and (c) **5** with the increase of Pb^{2+} concentration; Stern–Volmer linear fitting of I/I_0 to Pb^{2+} ions in the low concentration range in suspensions of complexes (b) **3** and (d) **5**.

To the best of our knowledge, complex **3** exhibits the lowest detection limit for Pb^{2+} ions among the existing complex fluorescent probes (Table S2†). In addition, complexes **3** and **5** represent attractive fluorescent-enhanced probes; they are more stable with respect to background interference during detection, and show low signal-to-noise ratio and higher sensitivity.

3.8 Cyclability performance and practical application of the sensor

Fluorescent detection materials must not only have a low detection limit, but their recoverability and detection performance in real samples are also very important. The fluorescence recovery properties of complexes **3** and **5** were investigated after interaction with Pb^{2+} ions. As shown in Fig. 10, the fluorescence intensity of complexes **3** and **5** after interacting with Pb^{2+} can be well restored by washing, indicating that the complexes can be employed repeatedly for at least five times as fluorescent probes for Pb^{2+}.

To verify the feasibility of the sensors for practical applications, the detection performance of complexes **3** and **5** for Pb^{2+} ions were investigated in tap water and river water (pre-

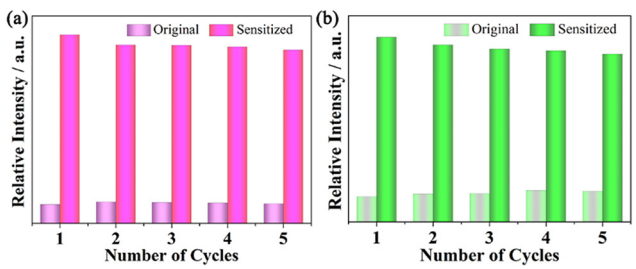

Fig. 10 The fluorescence intensity of complexes (a) **3** and (b) **5** for detection of Pb^{2+} after five recycling experiments (λ_{em} = 613 nm for **3**, λ_{em} = 543 nm for **5**).

pared from Fenhe River in Shanxi Province of China). As shown in Table S3,† the concentrations of Pb^{2+} ions in tap and river water detected by complexes **3** and **5** agree well with the ICP-MS results. Therefore, complexes **3** and **5** show good potential for the detection of Pb^{2+} ions in practical applications.

3.9 Sensing mechanisms

Three possible mechanisms by which Pb^{2+} ions can enhance the fluorescence of a complex are feasible:[53–56] (a) the structure of the complex itself may change; (b) the complex adsorbs Pb^{2+} ions, resulting in fluorescence changes; (c) the interaction of Pb^{2+} ions with the complex leads to energy transfer. Mechanistic studies were carried out to distinguish experimentally between these potential mechanisms. As shown in Fig. S9,† PXRD results indicate that the structures of complexes **3** and **5** do not change before and after immersion in Pb^{2+} aqueous solutions with a concentration of 0.01 M, showing that their structures have not changed, which is different from the mechanism reported in the literature.[42] ICP results (Table S4†) prove that complexes **3** and **5** are doped with only a very small amount of lead after immersion in aqueous solutions of Pb^{2+} ions with a concentration of 0.01 M; a mechanism involving adsorption of Pb^{2+} ion can therefore be ruled out.

The XPS spectra (Fig. S10†) show that after the detection of Pb^{2+} ions, two new peaks are observed at 143.17 and 138.29 eV in complex **3**; they can be attributed to Pb $4f_{5/2}$ and Pb $4f_{7/2}$, respectively. Two similar peaks appear in complex **5** at 143.28 and 138.39 eV after the detection. In addition, the binding energies of Eu $3d_{5/2}$ and $3d_{3/2}$ in complex **3** and Tb $3d_{5/2}$ and $3d_{3/2}$ in complex **5** consistently shift to higher energies (Eu $3d_{3/2}$ from 1164.53 to 1164.58 eV, Eu $3d_{5/2}$ from 1135.08 to 1135.18 eV, Tb $3d_{3/2}$ from 1276.81 to 1276.89 eV and Tb $3d_{5/2}$ from 1241.67 to 1242.61 eV). In parallel, the binding energies of the O 1*s* in the complexes are also slightly blue-shifted. In complex **3**, the binding energies at 532.98 eV (ether-oxygen bond) and 531.58 eV (Eu–O bond) decrease to 532.89 and 531.29 eV respectively, while in complex **5**, the binding energies at 533.08 eV (ether-oxygen bond) and 531.42 eV (Tb–O bond) shift to 532.98 and 531.22 eV. These results indicate interactions between Pb^{2+} ions and the ligand in which the ether-oxygen and uncoordinated carboxylate oxygen atoms may both act as Lewis basic sites, resulting in a more efficient charge transfer from the ligand to the Eu(III) and Tb(III) ions, and fluorescence enhancement.[53–58] More convincingly, the Eu(III) are more easily sensitized (17 300 cm^{-1}) than the Tb(III) ion (20 500 cm^{-1}) due to its lower excited state energy,[59] thus the detection limit of Pb^{2+} ions for europium complex **3** is lower than that of terbium complex **5**.

Compared to other ions, the heavy metal ion Pb^{2+}, with the s^2 electronic configuration, has the higher atomic number, so it can effectively overlap with the electronic energy levels of the ligand, thus enhancing spin–orbit coupling and effectively achieving intersystemic crossover (ISC) of triplet states in the ligand. Therefore, Pb^{2+} can minimize the non-radiative loss of triple exciton and improve the ISC efficiency,[13,60,61] which promotes efficient energy transfer from the ligand to Eu(III) and Tb(III) ions. In addition, the delocalized between π bonds of the aromatic carboxylate groups and the s and p orbitals of the Pb^{2+} center can effectively interact to enable ligand-to-metal charge transfer (LMCT), thus making it easier to transfer energy from the ligand that absorbs the excited light energy to the metal center.[62,63]

4. Conclusions

In summary, six novel lanthanide complexes of the ligand 4,5-di(3,5-dicarboxylphenoxy)phthalic acid were synthesized by hydrothermal methods and their structures were characterized in detail. Based on the red, blue and green emission of the Eu, Gd and Tb complexes, a white light-emitting ternary Eu/Gd/Tb complex was synthesized. At an excitation wavelength of 380 nm, its CIE coordinate is (0.330, 0.339), close to pure white light emission. Fluorescence detection showed that Pb^{2+} ions can selectively enhance the fluorescence intensity of the Eu and Tb complexes in aqueous solutions with low detection limits of 4.72 nM and 49.75 nM, respectively, and the fluorescence enhancement can be perceived with the naked eye. To the best of our knowledge, the Eu complex exhibits the lowest detection limit for Pb^{2+} ions among the systems hitherto described. The corresponding fluorescence enhancement mechanism suggests interactions between the Pb^{2+} ion and the ether-oxygen and uncoordinated carboxylate oxygen on the ligand, leading to a more efficient transfer of charge on the ligand to the Eu(III) and Tb(III) ions, which enhance the fluorescence. In conclusion, the Eu and Tb complexes have great potential for application in the detection of Pb^{2+} ions in real water.

Author contributions

Wenwen Wei: experiments, formal analysis, writing – original draft. Ai Wang: review & editing. Li Ping Lu: funding acquisition. Caixia Yuan: review & editing. Sisi Feng: supervision, funding acquisition, writing – review & editing, project administration. Ulli Englert: validated the experimental data, writing –review & editing. Shengqian Ma: review & editing.

Conflicts of interest

There are no conflicts to declare.

Acknowledgements

This work was supported financially by the National Natural Science Foundation of China (Grant No. 22073058), the Natural Science Foundation of Shanxi Province (202303021211017), the Shanxi Scholarship Council of China

(2023-004 & 2023-018); this work was in part performed at the Scientific Instrument Center of Shanxi University of China.

References

1 Y. Gao, Y. Jiao, H. Zhang, W. Lu, Y. Liu, H. Han, X. Gong, L. Li, S. Shuang and C. Dong, One-step synthesis of a dual-emitting carbon dot-based ratiometric fluorescent probe for the visual assay of Pb^{2+} and PPi and development of a paper sensor, *J. Mater. Chem. B*, 2019, **7**, 5502–5509.

2 W. Guo, C. Zhang, T. Ma, X. Liu, Z. Chen, S. Li and Y. Deng, Advances in aptamer screening and aptasensors' detection of heavy metal ions, *J. Nanobiotechnol.*, 2021, **19**, 166.

3 Y. Jiang, Y. Wang, F. Meng, B. Wang, Y. Cheng and C. Zhu, N-doped carbon dots synthesized by rapid microwave irradiation as highly fluorescent probes for Pb^{2+} detection, *New J. Chem.*, 2015, **39**, 3357–3360.

4 Y. Liu, Q. Zhou, J. Li, M. Lei and X. Yan, Selective and sensitive chemosensor for lead ions using fluorescent carbon dots prepared from chocolate by one-step hydrothermal method, *Sens. Actuators, B*, 2016, **237**, 597–604.

5 N. A. A. Qasem, R. H. Mohammed and D. U. Lawal, Removal of heavy metal ions from wastewater: a comprehensive and critical review, *npj Clean Water*, 2021, **4**, 36.

6 X. Wang, H. Guo, N. Wu, M. Xu, L. Zhang and W. Yang, A dual-emission fluorescence sensor constructed by encapsulating double carbon dots in zeolite imidazole frameworks for sensing Pb^{2+}, *Colloids Surf., A*, 2021, **615**, 126218.

7 J. Xu, X. Jie, F. Xie, H. Yang, W. Wei and Z. Xia, Flavonoid moiety-incorporated carbon dots for ultrasensitive and highly selective fluorescence detection and removal of Pb^{2+}, *Nano Res.*, 2018, **11**, 3648–3657.

8 L. Järup, Hazards of heavy metal contamination, *Br. Med. Bull.*, 2003, **68**, 167–182.

9 J. E. Johnston, M. Franklin, H. Roh, C. Austin and M. Arora, Lead and Arsenic in Shed Deciduous Teeth of Children Living Near a Lead-Acid Battery Smelter, *Environ. Sci. Technol.*, 2019, **53**, 6000–6006.

10 A. Kumar, A. R. Chowdhuri, D. Laha, T. K. Mahto, P. Karmakar and S. K. Sahu, Green synthesis of carbon dots from Ocimum sanctum for effective fluorescent sensing of Pb^{2+} ions and live cell imaging, *Sens. Actuators, B*, 2017, **242**, 679–686.

11 J. F. Olorunyomi, J. F. White, T. R. Gengenbach, R. A. Caruso and C. M. Doherty, Fabrication of a Reusable Carbon Dot/Gold Nanoparticle/Metal–Organic Framework Film for Fluorescence Detection of Lead Ions in Water, *ACS Appl. Mater. Interfaces*, 2022, **14**, 35755–35768.

12 A. D. Pournara, C.-G. Bika, X. Chen, T. Lazarides, S. Kaziannis, P. Feng and M. J. Manos, A bifunctional robust metal sulfide with highly selective capture of Pb^{2+} ions and luminescence sensing ability for heavy metals in aqueous media, *Inorg. Chem. Front.*, 2021, **8**, 4052–4061.

13 S. Xu, L. Zhan, C. Hong, X. Chen, X. Chen and M. Oyama, Metal–organic framework-5 as a novel phosphorescent probe for the highly selective and sensitive detection of Pb(II) in mussels, *Sens. Actuators, B*, 2020, **308**, 127733.

14 S. H. K. Yap, Y.-H. Chien, R. Tan, A. R. bin Shaik Alauddin, W. B. Ji, S. C. Tjin and K.-T. Yong, An Advanced Hand-Held Microfiber-Based Sensor for Ultrasensitive Lead Ion Detection, *ACS Sens.*, 2018, **3**, 2506–2512.

15 A. H. Gore, D. B. Gunjal, M. R. Kokate, V. Sudarsan, P. V. Anbhule, S. R. Patil and G. B. Kolekar, Highly Selective and Sensitive Recognition of Cobalt(II) Ions Directly in Aqueous Solution Using Carboxyl-Functionalized CdS Quantum Dots as a Naked Eye Colorimetric Probe: Applications to Environmental Analysis, *ACS Appl. Mater. Interfaces*, 2012, **4**, 5217–5226.

16 Y. Huang, Y. Ma, Y. Chen, X. Wu, L. Fang, Z. Zhu and C. J. Yang, Target-Responsive DNAzyme Cross-Linked Hydrogel for Visual Quantitative Detection of Lead, *Anal. Chem.*, 2014, **86**, 11434–11439.

17 Y. Liu, Q. Zhou, Y. Yuan and Y. Wu, Hydrothermal synthesis of fluorescent carbon dots from sodium citrate and polyacrylamide and their highly selective detection of lead and pyrophosphate, *Carbon*, 2017, **115**, 550–560.

18 L. Wang, B. Li, J. Wang, J. Qi, J. Li, J. Ma and L. Chen, A rotary multi-positioned cloth/paper hybrid microfluidic device for simultaneous fluorescence sensing of mercury and lead ions by using ion imprinted technologies, *J. Hazard. Mater.*, 2022, **428**, 128165.

19 L. E. MacKenzie and R. Pal, Circularly polarized lanthanide luminescence for advanced security inks, *Nat. Rev. Chem.*, 2020, **5**, 109–124.

20 K. Nehra, A. Dalal, A. Hooda, P. Kumar, D. Singh, S. Kumar, R. S. Malik and P. Kumar, Luminous terbium and samarium complexes with diacetylmethane and substituted 1,10-phenanthroline derivatives for display applications: Preparation and optoelectronic investigations, *J. Lumin.*, 2022, **249**, 119032.

21 D. Parker, J. D. Fradgley and K.-L. Wong, The design of responsive luminescent lanthanide probes and sensors, *Chem. Soc. Rev.*, 2021, **50**, 8193–8213.

22 M. Wei, L. Luo, R. Cui, X. Wang, J. Chen, Z. Cai, X. Li, H. Wei, C. Wei and Z. Bian, Highly luminescent and stable lanthanide coordination polymers based 2-(3′,4′-dicarboxyphenoxy)-benzoic acid: Crystal structure, photoluminescence, white light emission and fluorescence sensing, *Dyes Pigm.*, 2022, **206**, 110650.

23 Y. Li, S. Zhang and D. Song, A Luminescent Metal-Organic Framework as a Turn-On Sensor for DMF Vapor, *Angew. Chem., Int. Ed.*, 2013, **52**, 710–713.

24 J. Ren, Z. Niu, Y. Ye, C. Y. Tsai, S. Liu, Q. Liu, X. Huang, A. Nafady and S. Ma, Second–Sphere Interaction Promoted Turn–On Fluorescence for Selective Sensing of Organic Amines in a TbIII–based Macrocyclic Framework, *Angew. Chem., Int. Ed.*, 2021, **60**, 23705–23712.

25 Y. Abraham, H. Salman, K. Suwinska and Y. Eichen, Cyclo [2]benzimidazole: luminescence turn-on sensing of anions, *Chem. Commun.*, 2011, **47**, 6087–6089.
26 B. Chen, L. Wang, F. Zapata, G. Qian and E. B. Lobkovsky, A Luminescent Microporous Metal-Organic Framework for the Recognition and Sensing of Anions, *J. Am. Chem. Soc.*, 2008, **130**, 6718–6719.
27 T.-Y. Luo, P. Das, D. L. White, C. Liu, A. Star and N. L. Rosi, Luminescence "Turn-On" Detection of Gossypol Using Ln^{3+}-Based Metal–Organic Frameworks and Ln^{3+} Salts, *J. Am. Chem. Soc.*, 2020, **142**, 2897–2904.
28 D. Wu, Z. Zhang, X. Chen, L. Meng, C. Li, G. Li, X. Chen, Z. Shi and S. Feng, A non-luminescent Eu-MOF-based "turn-on" sensor towards an anthrax biomarker through single-crystal to single-crystal phase transition, *Chem. Commun.*, 2019, **55**, 14918–14921.
29 H.-Q. Yin, X.-Y. Wang and X.-B. Yin, Rotation Restricted Emission and Antenna Effect in Single Metal–Organic Frameworks, *J. Am. Chem. Soc.*, 2019, **141**, 15166–15173.
30 A. K. Chaudhari, S. S. Nagarkar, B. Joarder and S. K. Ghosh, A Continuous π-Stacked Starfish Array of Two-Dimensional Luminescent MOF for Detection of Nitro Explosives, *Cryst. Growth Des.*, 2013, **13**, 3716–3721.
31 J. Chen, H. Zhang, B. Li, J. Yang, X. Li, T. Zhang, C. He, C. Duan and L. Wang, Bioinspired Carboxylate–Water Coordination Polymers with Hydrogen-Bond Clusters and Local Coordination Flexibility for Electrochemical Water Splitting, *ACS Appl. Energy Mater.*, 2020, **3**, 10515–10524.
32 Q. Luo, Z. Zhu, C. Fan, Z. a. Zong, C. Xu, C. Bi and Y. Fan, Two dia isomorphic Zn-MOFs based on two isomeric semi-rigid aromatic tetracarboxylate acids: Syntheses and properties, *J. Mol. Struct.*, 2019, **1188**, 57–61.
33 K. K. Wan, J. H. Yu, Q. F. Yang and J. Q. Xu, 5,5′–(1,4−Dioxo−1,2,3,4−tetrahydrophthalazine−6,7−diyl)bis (oxy)diisophthalate–Based Coordination Polymers and their TNP Sensing Ability, *Eur. J. Inorg. Chem.*, 2019, **2019**, 3094–3102.
34 J.-M. Wang, P.-F. Zhang, J.-G. Cheng, Y. Wang, L.-L. Ma, G.-P. Yang and Y.-Y. Wang, Luminescence tuning and sensing properties of stable 2D lanthanide metal–organic frameworks built with symmetrical flexible tricarboxylic acid ligands containing ether oxygen bonds, *CrystEngComm*, 2021, **23**, 411–418.
35 Y. Wang, H.-M. Zeng, W.-T. Mao, X.-J. Wang, Z.-G. Jiang, C.-H. Zhan and Y.-L. Feng, The synthesis and photoluminescence of three porous metal-organic frameworks, *Inorg. Chem. Commun.*, 2021, **129**, 108613.
36 M.-Y. Zhang, R.-D. Dai, B.-J. Li, T.-X. Hang, J.-X. Xie, J. Lü and X.-D. Zhu, Fluorescent Metal–Organic Framework Constructed from Semi-rigid Ligand for the Sensitive Sensing of 2,4,6-Trinitrophenol, *Cryst. Growth Des.*, 2020, **20**, 1373–1377.
37 X. Feng, Y. Feng, N. Guo, Y. Sun, T. Zhang, L. Ma and L. Wang, Series d–f Heteronuclear Metal–Organic Frameworks: Color Tunability and Luminescent Probe with Switchable Properties, *Inorg. Chem.*, 2017, **56**, 1713–1721.
38 G. Ji, J. Liu, X. Gao, W. Sun, J. Wang, S. Zhao and Z. Liu, A luminescent lanthanide MOF for selectively and ultra-high sensitively detecting Pb^{2+} ions in aqueous solution, *J. Mater. Chem. A*, 2017, **5**, 10200–10205.
39 L. Li, Q. Chen, Z. Niu, X. Zhou, T. Yang and W. Huang, Lanthanide metal–organic frameworks assembled from a fluorene-based ligand: selective sensing of Pb^{2+} and Fe^{3+} ions, *J. Mater. Chem. C*, 2016, **4**, 1900–1905.
40 W. Liu, X. Dai, Z. Bai, Y. Wang, Z. Yang, L. Zhang, L. Xu, L. Chen, Y. Li, D. Gui, J. Diwu, J. Wang, R. Zhou, Z. Chai and S. Wang, Highly Sensitive and Selective Uranium Detection in Natural Water Systems Using a Luminescent Mesoporous Metal–Organic Framework Equipped with Abundant Lewis Basic Sites: A Combined Batch, X-ray Absorption Spectroscopy, and First Principles Simulation Investigation, *Environ. Sci. Technol.*, 2017, **51**, 3911–3921.
41 H. Xu, S. Zhou, L. Xiao, H. Wang, S. Li and Q. Yuan, Fabrication of a nitrogen-doped graphene quantum dot from MOF-derived porous carbon and its application for highly selective fluorescence detection of Fe^{3+}, *J. Mater. Chem. C*, 2015, **3**, 291–297.
42 Z. Cong, M. Zhu, Y. Zhang, W. Yao, M. Kosinova, V. P. Fedin, S. Wu and E. Gao, Three novel metal-organic frameworks with different coordination modes for trace detection of anthrax biomarkers, *Dalton Trans.*, 2021, **51**, 250–256.
43 Y. Ma, Z. Zhao, M. Zhu, Y. Zhang, M. Kosinova, V. P. Fedin, S. Wu and E. Gao, Rapid detection of lamotrigine by a water stable fluorescent lanthanide metal–organic framework sensor, *Polyhedron*, 2022, **220**, 115803.
44 Y. Ma, M. Zhu, Y. Zhang, Y. Sun and S. Wu, A water-stable Eu-MOF as multi-responsive luminescent sensor for high-efficiency detection of Fe^{3+}, MnO_4^- ions and nicosulfuron in aqueous solution, *J. Solid State Chem.*, 2022, **316**, 123598.
45 G. M. Sheldrick, *SADABS: Empirical Absorption Correction Program*, University of Gottingen, Gottingen, Germany, 1997.
46 G. M. Sheldrick, SHELXT - integrated space-group and crystal-structure determination, *Acta Crystallogr., Sect. A: Found. Adv.*, 2015, **71**, 3–8.
47 O. V. Dolomanov, L. J. Bourhis, R. J. Gildea, J. A. K. Howard and H. Puschmann, *J. Appl. Crystallogr.*, 2009, **42**, 339–341.
48 G. M. Sheldrick, Crystal structure refinement with SHELXL, *Acta Crystallogr., Sect. C: Struct. Chem.*, 2015, **71**, 3–8.
49 K. Gholivand, M. Hosseini, Y. Maghsoud, J. Valenta, A. A. Ebrahimi Valmuzi, A. Owczarzak, M. Kubicki, M. Jamshidi and M. Kahnouji, Relations between Structural and Luminescence Properties of Novel Lanthanide Nitrate Complexes with Bis-phosphoramidate Ligands, *Inorg. Chem.*, 2019, **58**, 5630–5645.
50 T. Kumar, A. Karmakar, A. Halder and R. R. Koner, Ni(II)-Based Coordination Polymer with Pi-Conjugated Organic Linker as Catalyst for Oxygen Evolution Reaction Activity, *Energy Fuels*, 2022, **36**, 2722–2730.

51 R. Wang, H. Xiang, J. Chen, Y. Li, Y. Zhou, W. C. H. Choy, Z. Fan and H. Zeng, Energy Regulation in White-Light-Emitting Diodes, *ACS Energy Lett.*, 2022, **7**, 2173–2188.

52 M. X. Yu, C. P. Liu, Y. F. Zhao, S. C. Li, Y. L. Yu, J. Q. Lv, L. Chen, F. L. Jiang and M. C. Hong, White–Light Emission and Circularly Polarized Luminescence from a Chiral Copper(I) Coordination Polymer through Symmetry–Breaking Crystallization, *Angew. Chem., Int. Ed.*, 2022, **61**, e202201590.

53 X. An, Q. Tan, S. Pan, H. Liu and X. Hu, A turn-on luminescence probe based on amino-functionalized metal-organic frameworks for the selective detections of Cu^{2+}, Pb^{2+} and pyrophosphate, *Spectrochim. Acta, Part A*, 2021, **247**, 19073.

54 K. Hanaoka, K. Kikuchi, H. Kojima, Y. Urano and T. Nagano, Selective Detection of Zinc Ions with Novel Luminescent Lanthanide Probes, *Angew. Chem., Int. Ed.*, 2003, **42**, 2996–2999.

55 Z. Li, Z. Zhan and M. Hu, A luminescent terbium coordination polymer as a multifunctional water-stable sensor for detection of Pb^{2+} ions, PO_4^{3-} ions, $Cr_2O_7^{2-}$ ions, and some amino acids, *CrystEngComm*, 2020, **22**, 6727–6737.

56 M. Wang, L. Guo and D. Cao, Metal-organic framework as luminescence turn-on sensor for selective detection of metal ions: Absorbance caused enhancement mechanism, *Sens. Actuators, B*, 2018, **256**, 839–845.

57 W. Gao, A.-M. Zhou, H. Wei, C.-L. Wang, J.-P. Liu and X.-M. Zhang, Water-stable LnIII-based coordination polymers displaying slow magnetic relaxation and luminescence sensing properties, *New J. Chem.*, 2020, **44**, 6747–6759.

58 G. Ji, X. Gao, T. Zheng, W. Guan, H. Liu and Z. Liu, Postsynthetic Metalation Metal–Organic Framework as a Fluorescent Probe for the Ultrasensitive and Reversible Detection of PO_4^{3-} Ions, *Inorg. Chem.*, 2018, **57**, 10525–10532.

59 G. Liu, Y.-K. Lu, Y.-Y. Ma, X.-Q. Wang, L. Hou and Y.-Y. Wang, Syntheses of three new isostructural lanthanide coordination polymers with tunable emission colours through bimetallic doping, and their luminescence sensing properties, *Dalton Trans.*, 2019, **48**, 13607–13613.

60 Q.-B. Bo, J.-J. Pang, H.-Y. Wang, C.-H. Fan and Z.-W. Zhang, In situ solvent and counteranion-induced synthesis, structural characterization and photoluminescence properties of Pb-based MOFs, *New J. Chem.*, 2015, **39**, 431–438.

61 M. Pan, C. Yan, L. Chen, L.-Y. Zhang, S.-Y. Yin, Y.-X. Zhu, K. Wu, Y.-J. Hou and C.-Y. Su, Photoluminescence and white-light emission in two series of heteronuclear Pb(II)–Ln(III) complexes, *New J. Chem.*, 2015, **39**, 3770–3776.

62 Y. Jiang, Y. Wang, F. Meng, B. Wang, Y. Cheng and C. Zhu, N-doped carbon dots synthesized by rapid microwave irradiation as highly fluorescent probes for Pb^{2+} detection, *New J. Chem.*, 2015, **39**, 3357–3360.

63 J. Yang, G. D. Li, J. J. Cao, Q. Yue, G. H. Li and J. S. Chen, Structural variation from 1D to 3D: effects of ligands and solvents on the construction of lead(II)-organic coordination polymers, *Chem. – Eur. J.*, 2007, **13**, 3248–3261.